buildings

MDPI

Article

Seismic Analysis of Non-Regular Structures Based on Fragility Curves: A Study on Reinforced Concrete Frames †

Giovanni Smiroldo, Marco Fasan and Chiara Bedon *

Department of Engineering and Architecture, University of Trieste, Via Valerio 6/1, 34127 Trieste, Italy; giovanni.smiroldo@phd.units.it (G.S.); mfasan@units.it (M.F.)

* Correspondence: chiara.bedon@dia.units.it; Tel.: +39-040-558 3937

† This paper is an extended version of our paper published in: Smiroldo, G.; Fasan, M.; Bedon, C. Non-regularity damage evaluation in reinforced concrete structures via fragility curves. In Proceedings of the 64th International Conference on Vibroengineering, Trieste, Italy, 21–22 September 2023.

Abstract: The seismic performance and expected structural damage in reinforced concrete (RC) frames, as in many others, is a critical aspect for design. In this study, a set of RC frames characterized by increasing in-plan and in-height non-regularity is specifically investigated. Four code-conforming three-dimensional (3D) buildings with varying regularity levels are numerically analyzed. Their seismic assessment is conducted by using unscaled real ground motion records (61 in total) and employing non-linear dynamic simulations within the Cloud Analysis framework. Three distinct intensity measures (*IMs*) are used to evaluate the impact of structural non-regularity on their seismic performance. Furthermore, fragility curves are preliminary derived based on conventional linear regression models and lognormal distribution. In contrast with the initial expectations and the typical results of non-linear dynamic analyses, the presented comparative results of the fragility curves show that the non-regularity level increase for the examined RC frames does not lead to progressively increasing fragility. Upon these considerations on the initial numerical findings, a re-evaluation of the methodology is performed using a reduced subset of ground motion records, in order to account for potential biases in their selection. Moreover, to uncover deeper insights into the unexpected outcomes, a logistic regression based on a maximum likelihood estimate is also employed to develop fragility curves. Comparative results are thus critically discussed, showing that the herein considered fragility development methods may lead to seismic assessment outcomes for code-conforming non-regular buildings that are in contrast with those of raw structural analyses. In fact, the considered building code design provisions seem to compensate non-regularity-induced torsional effects.

Keywords: reinforced concrete; non-regularity; seismic analysis; numerical modeling; Cloud Analysis; fragility curves

Citation: Smiroldo, G.; Fasan, M.; Bedon, C. Seismic Analysis of Non-Regular Structures Based on Fragility Curves: A Study on Reinforced Concrete Frames. *Buildings* **2024**, *14*, 3734. https://doi.org/10.3390/buildings14123734

Academic Editor: Binsheng (Ben) Zhang

Received: 16 October 2024
Revised: 21 November 2024
Accepted: 21 November 2024
Published: 23 November 2024

1. Introduction

As is known, the dynamic behavior of structures is significantly influenced by both in-plan and in-height non-regularity features. For a given structural system under seismic loading, in general terms, in-plan non-regularity can lead to unfavorable torsional effects, while in-height non-regularity typically impacts the modal participation of higher vibration modes [1,2]. Post-earthquake damage assessments have highlighted the presence of torsional effects induced by non-regularity in building layouts, including those in reinforced concrete (RC) buildings. Most of these RC buildings were primarily designed to withstand gravity loads and were constructed between the 1950s and 1980s [3–6], a period preceding the widespread integration of seismic design considerations into building codes, which began in the 1990s and early 2000s. Currently, to minimize such structural issues, various international building and structural codes address these regularity aspects based on different strategies and design assumptions [7–9], but often do not consider them from a risk assessment perspective.

The fragility assessment of non-regular buildings is usually carried out using damage data collected in the aftermath of earthquakes, in order to determine the classical empirical and typological fragility curves [10–12]. While there has been a large amount of effort in evaluating torsional effects on existing buildings (e.g., [13–15]), an increasing interest in code-conforming irregular RC building is noted, with more classic L-shaped buildings [16–18]. This study, in this regard, aims to assess the possible damage effects that are commonly associated with in-plan and in-height non-regularities by developing fragility curves within the framework of Cloud Analysis [19–21], for a selection of code-conforming structural systems of technical interest. To achieve this goal, four reinforced concrete (RC) frames are designed, based on technical provisions from the Italian building code [4], assuming that they are located in a high-seismicity zone. These structural layouts are intentionally designed to exhibit different levels of non-regularity, which is quantified using the Torsional Irregularity Ratio (TIR), see ref. [22].

Remarkably, despite the major differences in the non-regularities of the case-study systems, all these structures are designed to show a comparable distribution of demand-to-capacity ratios, in order to avoid possible bias coming from an initial over-sizing. Their seismic performance assessment is thus critically discussed in terms of fragility. Interestingly, the detailed analysis of the numerical comparative results shows that the selected methods for the definition of fragility curves may lead to seismic assessment outcomes that—for non-regular buildings—are in contrast with raw structural analyses: this is probably due to building code provisions that, from a design point of view, effectively account for torsional effects by increasing the input spectral acceleration. Therefore, it is suggested that further investigations and efforts are necessary in this area, as the considered building code may, to some extent, over-compensate for the adverse effects introduced by non-regularity.

2. Examined RC Structures and Method of Analysis

2.1. Preliminary Design Assumptions

The four reference structures consist of three different multi-storey RC frame layouts, each of which is characterized by a different regularity [23] (see Figure 1).

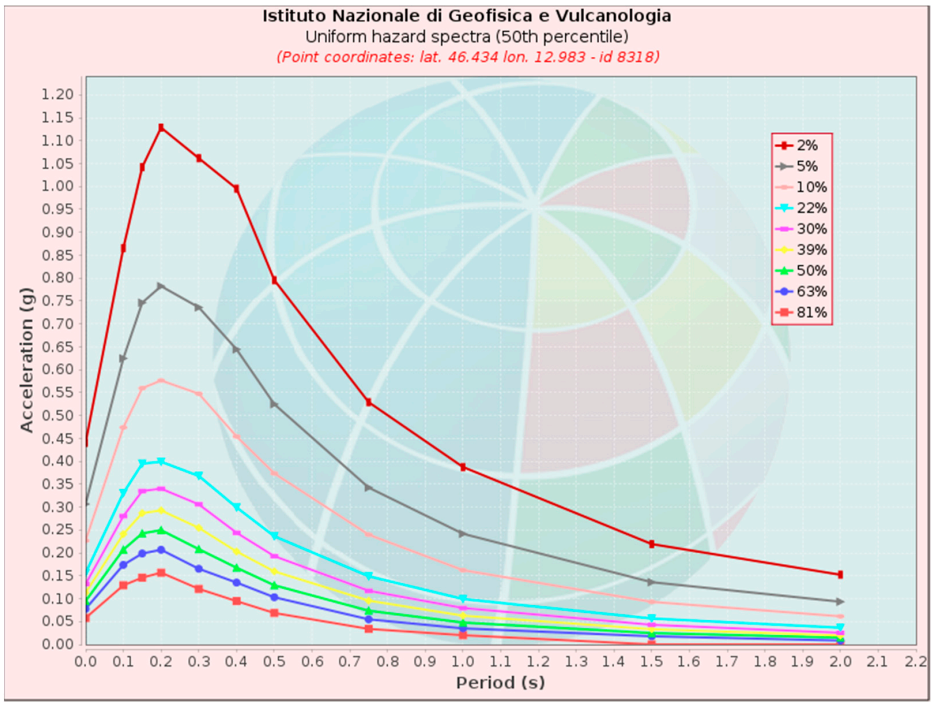

Figure 1. Hazard spectra for Tolmezzo (Udine, Italy) site.

The first structural system, herein referred to as "Regular Frame" (RF), features a square plan measuring 15 m in width, and is divided into three bays, each with a length of

5 m. The height of each storey is 3 m, resulting in a total height of 15 m. Concrete of strength class C28/35 is used for beams and columns, along with B450C steel rebars. Permanent gravitational loads encompass the structural weight of the building components, with a load of 3.12 kN/m^2, which is attributed to the floors of the structural system (RC slabs), and 2.8 kN/m^2 for the roof floor. A live load of 2 kN/m^2 is also considered as uniformly distributed on each floor. Furthermore, the roof floor is designed to accommodate a live snow load of 0.8 kN/m^2, with no partitions. Seismic input is finally defined in accordance with the Italian building code [8] for Tolmezzo (Udine) site, a high-seismicity location in the northeastern part of Italy. The elastic spectra (with different rates of exceedance relative to the Limit States) used in the design process are shown in Figure 1.

Using the hazard spectrum corresponding to the rate of exceedance equal to 10%, a response spectrum analysis is employed to determine the maximum stress values within beams and columns. All three structures adhere to the "weak beam/strong column" capacity design criterion. Shear forces in members are evaluated based on the flexural capacity of their critical regions, thus averting shear-related failures. In terms of boundaries and constraints, floors are treated as rigid diaphragms for the 3D assemblies, while fixed supports are applied at the base nodes.

For the sake of clarity, beams and column cross-sections of the Regular Frame are illustrated in Figure 2. Full details of rebar percentages for the load-bearing elements, of all reference buildings, can be provided upon request. Figure 2a, in particular, shows the column cross-section (50 cm × 50 cm its size) for floors 1–2–3, for which rebars are defined by 12ϕ20 and ϕ10/10 cm shear rebars. In Figure 2b, the column cross-section (45 cm × 45 cm) for floors 4 and 5 is presented, for which rebars are defined by 4ϕ20 in the corners and 4ϕ18 at the sides, with ϕ10/10 cm shear rebars. Figure 2c illustrates a perimetral beam cross-section (with dimensions of 40 cm × 30 cm), whose rebars are constituted by upper 2ϕ16 + 3ϕ18 and lower 3ϕ16, with shear rebars of ϕ8/8 cm. Finally, Figure 2d illustrates an internal beam cross-section (with dimensions of 25 cm × 50 cm) in which rebars are defined by 4ϕ16 both superiorly and inferiorly, with shear rebars of ϕ8/8 cm. All these elements have unconfined concrete width equal to 3 cm.

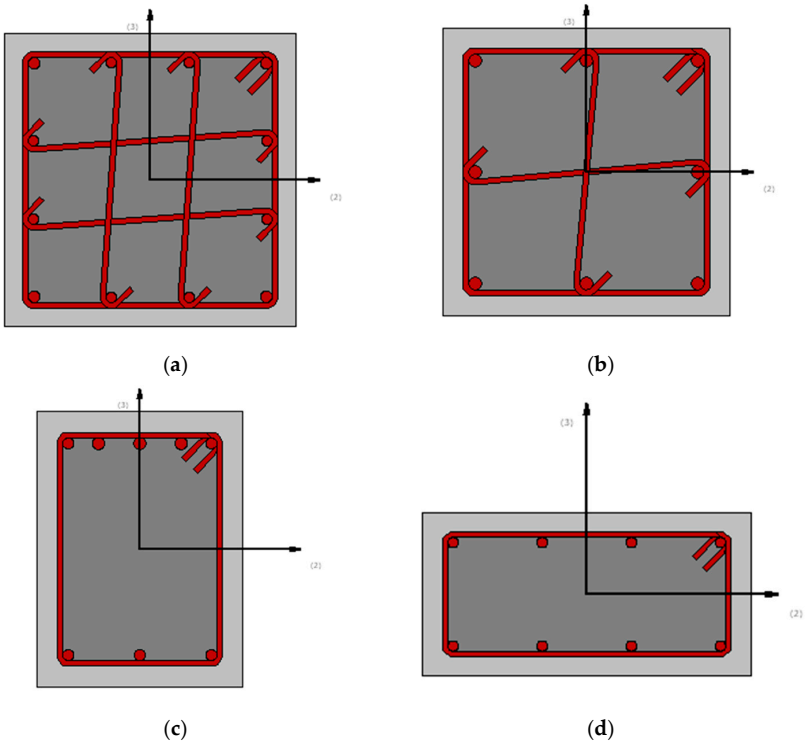

Figure 2. RF element cross-section: (**a**) 1–2–3 floors; (**b**) 4–5 columns; (**c**) perimetral and (**d**) internal beam.

Figure 3 shows the different layouts of the reference buildings, while Table 1 summarises their fundamental vibration periods.

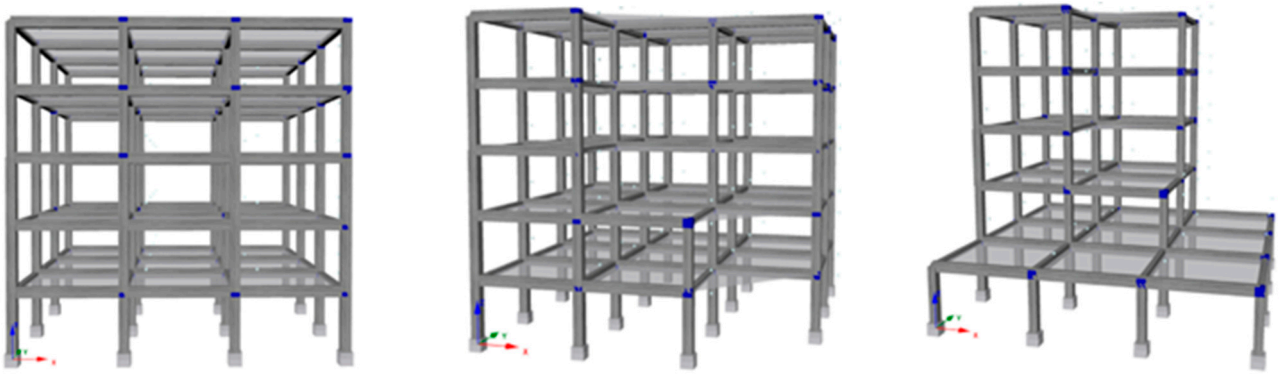

(**a**) (**b**) (**c**)

Figure 3. Reference structures: (**a**) RF; (**b**) NRF1; and (**c**) NRF2.

Table 1. Main vibration periods of the reference structures.

Structure	Mode	Period [s]	Ux	Uy	Rx	Ry	Rz
RF	1	0.881	0.00%	78.09%	9.33%	0.00%	0.00%
	2	0.753	80.29%	0.00%	0.00%	8.43%	0.00%
	3	0.677	0.00%	0.00%	0.00%	0.00%	80.02%
NRF1	1	0.816	0.00%	77.29%	10.38%	0.00%	0.01%
	2	0.729	75.60%	0.00%	0.00%	9.12%	3.14%
	3	0.650	2.50%	0.04%	0.00%	0.26%	74.61%
NRF2	1	0.681	2.73%	62.68%	16.52%	0.75%	5.09%
	2	0.626	59.73%	3.29%	0.95%	17.20%	5.45%
	3	0.499	2.96%	0.37%	0.16%	0.84%	38.82%

The geometries of both "Non-Regular Frame 1" (NRF1) and "Non-Regular Frame 2" (NRF2) structures are derived by removing beams and columns from the geometry of the RF, to finally obtain the desired level of non-regularity.

The primary objective of current research is, in fact, to assess the responses of the selected structures by varying their in-plan and in-height regularities. To achieve this goal, the structures necessarily need to closely align from a code–design perspective. The RF and NRF1 structures, in particular, are designed with a behaviour factor of 3.9. It is important to note that for torsionally deformable RC structures, the Italian code prescribes a behavior factor of 2 [8]. To address such a variance in the reference design criterion, the NRF2 structure is thus detailed in structural details using both approaches. Consequently, two torsionally deformable structures are analyzed, namely the NRF2-Q2 and NRF2-Q4 systems [24]. To quantify the degrees of irregularity in these buildings, the Torsional Irregularity Ratio (TIR) is employed, as defined in refs. [22,25]. TIR parameter, in particular, is calculated as the ratio of the maximum drift at the building edge to the average drift. The corresponding values for the presently examined structures are listed in Table 2, where it is possible to see the increasing irregularity degrees compared to RF.

Table 2. TIR values for the examined structural frames.

	RF	NRF1	NRF2
TIR	1	1.15	1.3

To accommodate design-related uncertainties, the outcomes of the response spectrum analysis are cross-verified, ensuring that all four structures show a comparable distribution of demand-to-capacity ratios. Figure 4 depicts the probability mass function of demand-to-bending-moment capacity ratios of beam sections. Notably, the verification intervals differ by increments of 0.1.

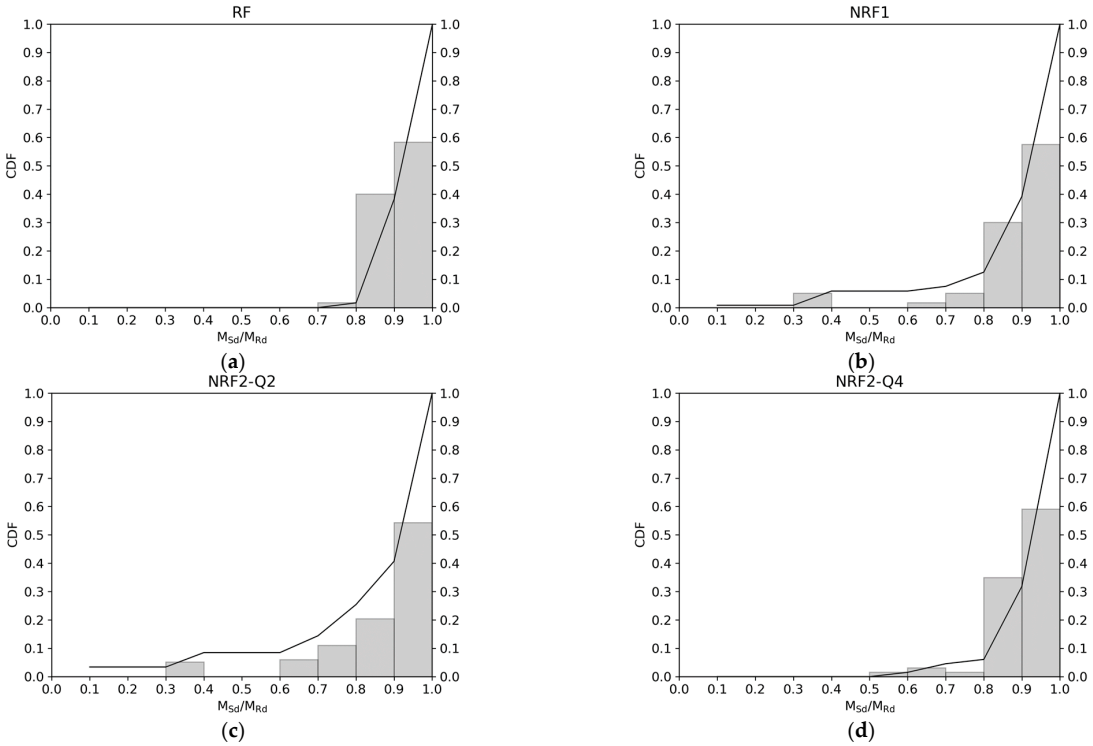

Figure 4. Verification intervals and cumulative distribution functions for the examined RC frames: (**a**) RF; (**b**) NRF1; (**c**) NRF2-Q2; and (**d**) NRF2-Q4.

Accompanying the histograms, Figure 4 also illustrates the discrete cumulative probability function. It is evident that a significant portion of the beams across all frames satisfies the verification within the demand/capacity ratio range of 0.8 to 0.9 for bending moment. The comparison among all the cumulative distribution functions is also shown in Figure 5. It can be noted that all cumulative distribution functions almost overlap for the 0.8–0.9 and 0.9–1.0 verification intervals, indicating that all the examined RC structures can be considered uniformly designed.

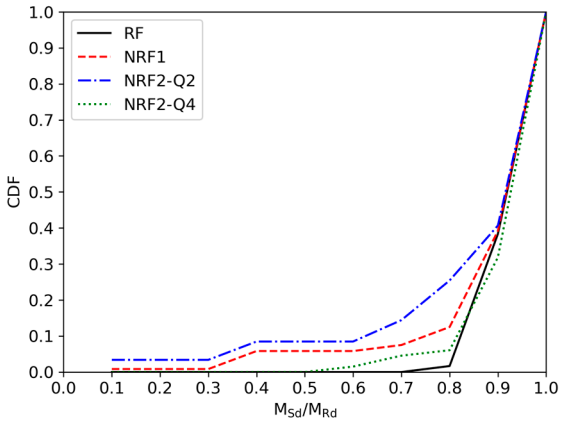

Figure 5. Comparison of cumulative distribution functions for the examined RC frames.

2.2. Structural Numerical Modeling

The examined buildings are meticulously modeled within the Finite Element Method (FEM) of Seismostruct software 2023 [26]. The typical model encompasses both geometric and material nonlinearities. In more detail, material nonlinearities are incorporated using a force-based inelastic frame element (*infrmFB*), which adopts a distributed plasticity model through fiber–section discretization [26]. Each beam element employs a total of 5 integration sections, with 150 discretized fibers, as shown in Figure 6.

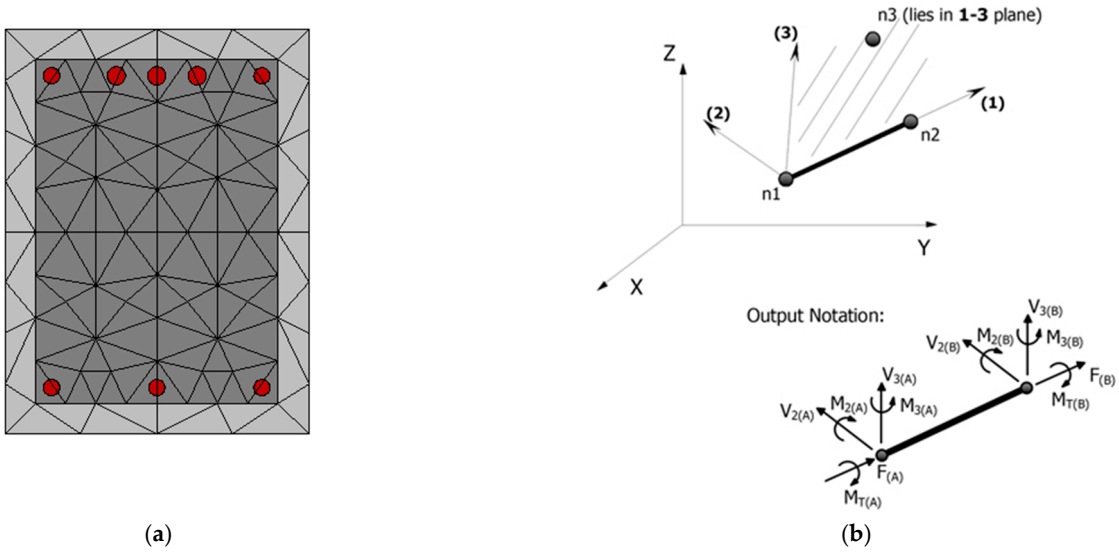

(**a**) (**b**)

Figure 6. infrmFB element: (**a**) fiber discretization; and (**b**) element orientation, with output notation.

In terms of concrete material, two constitutive laws are implemented, following the Mander model [27]: the first law pertains to the unconfined concrete in the cover and is characterized by a peak compressive strength (f_c) of 28 MPa at a strain (ε_{c0}) of 0.2%, and an ultimate strain (ε_{cu}) of 0.35%. The second law, applied to the concrete core, features a peak strength that varies based on the level of stirrup confinement (approximately 1.2 to 1.4 times the unconfined peak strength) and an ultimate strain value ε_{cu} = 0.8%. The reinforcement is represented using the Menegotto–Pinto constitutive law [28], with the mean yield strength f_y = 450 MPa (with a lower bound at 390 MPa) and a strain hardening parameter of 0.5%. The elastic moduli adopted for concrete and reinforcing steel are 32 GPa and 210 GPa, respectively.

As detailed in the Seismostruct manual [26], the simultaneous utilization of the diffused plasticity model and the rigid diaphragm constraint can lead to the generation of exceedingly high fictitious axial internal forces within the horizontal elements. To mitigate this possible interaction, beams are released from axial constraints through rigid links. These links are endowed with no axial stiffness and infinite stiffness in the other degrees of freedom [29].

Rayleigh damping is implemented in non-linear time history analyses (NLTHA). This notoriously necessitates the specification of two natural vibration periods, as well as a target damping factor for each of the chosen modes. These periods are judiciously selected to avert overdamping of higher modes and to account for elongated modes arising from plastic deformations. They correspond to 1.5 times the first natural vibration period and to the period leading to a cumulative mass participation ratio of 90%. The target damping factor is set at 3%, which is also in line with ASCE 2012 guidelines [30]. Finally, the Hilber–Hughes–Taylor integration scheme is employed for the analysis.

2.3. Seismic Analysis

The present approach involves conducting parametric NLTHAs using a selected set of 61 unscaled recorded ground motions. Given the three-dimensional nature of the reference

structures, NLTHAs are carried out using both horizontal components of the ground motion simultaneously.

For each record, three distinct Intensity Measures (*IMs*) are calculated to establish correlations between observed damage and input ground motion. As further detailed in the following sections, the chosen damage parameter is the demand/capacity ratio, which is computed in terms of chord rotation of the elements. Generally, fragility functions should be developed to account for uncertainties [31–34], including:

- Record-to-record variability;
- Variability in mechanical properties;
- Variability in performance level capacity thresholds;
- Model parameter variability.

The first three sources of uncertainty are primarily classified as aleatory, while the last is considered epistemic. The applied methodology inherently addresses record-to-record variability, as each (*IM*, *EDP*) pair in the Cloud originates from a distinct record. Additionally, although variabilities in the mechanical properties are not directly addressed in this study, they could be incorporated by sampling a different realization of the mechanical properties for each record, thereby enhancing the robustness of the fragility analysis.

Finally, to account for the statistical model parameter variability, a bootstrap procedure for each correlation is also used [35]. Subsequently, each linear regression realization yields a corresponding fragility curve. It is anticipated that the RC structures characterized by higher levels of non-regularity exhibit increased dispersion in the correlations.

After initial findings, it became apparent that the comparison of fragility curves did not align with the expected consistency or proportionality concerning the increment in non-regularity. This discrepancy was evident when examining the Engineering Demand Parameters (*EDPs*) derived from NLTHAs.

To address potential biases stemming from record selection, the entire methodology was entirely revised, by applying it to a reduced subset of accelerograms. However, even with the revised approach, the newly generated fragility curves continue to deviate from the anticipated relationship between structural damage and non-regularity. In response to this outcome, a different statistical model is thus employed, based on a maximum likelihood estimation, namely known as logistic regression [20]. This approach utilizes the Life Safety damage threshold exceeding as a binary condition. This adjustment, in present investigation, is aimed at better capturing the nuances of numerical data, and at potentially supporting a more detailed analysis of unexpected findings for non-regular buildings.

3. Seismic Performance Assessment

3.1. Intensity Measure Selection

To employ the Cloud Analysis procedure, the current study focuses on scalar intensity measures derived from recorded accelerograms. Given that structural models are inherently three-dimensional, each record needs to be represented by a bidirectional intensity measure (*IM*). Moreover, since the *IM* represents the unique link between hazard and fragility in a standard seismic risk evaluation, the *IM* ground motion component used in the two steps should be the same. In this study, the median geometric mean value across all feasible non-redundant rotation angles is utilized (*GMrotD50*), as it represents an emerging ground motion component in Ground Motion Prediction Equation [36].

Among scalar intensity measures, three are selected, characterized by being either structure-independent or structure-dependent, based on their reliance on the structural vibration properties. Among the structure-independent measures, Peak Ground Acceleration (PGA) stands out. In the realm of structure-dependent intensity measures, the spectral acceleration at the first mode ($S_a(T_1)$) is widely used. Given that both the reference structures and the NLTHAs are three-dimensional, the intensity measure needs to capture the principal vibration characteristics in both directions. Consequently, the spectral acceler-

ation is evaluated at an average period T_{1m}, defined as the mean of the fundamental period values in each direction (T_{1x} and T_{1y}, respectively) [22], as expressed in Equation (1):

$$S_a(T_{1m}) = S_a\left(\frac{T_{1x} + T_{1y}}{2}\right) \quad (1)$$

The third *IM* is represented by the spectral acceleration, evaluated as the geometric mean across a spectrum of periods T_i [37,38], as articulated in Equation (2):

$$S_{a,avg}(T_i) = \left[\prod_{i=1}^{n} S_a(T_i)\right]^{1/n} \quad (2)$$

This *IM*, more in detail, is adopted to take into account more effectively the rotational modes in non-regular structures, and, thus, it represents a highly efficient intensity measure [39–41].

The range of periods should be meticulously chosen to encompass the effects of higher modes and elongation of periods due to damage accumulation. In the present study, five periods are selected, as shown in Equation (3):

$$T_i = \left[T_{2m}, \min\left[\frac{T_{2m} + T_{1m}}{2}, 1.5{\cdot}T_{2m}\right], T_{1m}, 1.5{\cdot}T_{1m}, 2{\cdot}T_{1m}\right] \quad (3)$$

where T_{2m} is the mean of the second period across the two orthogonal directions.

3.2. Definition of Engineering Demand Parameter

In the context of assessing both structural and non-structural damage, the inter-storey drift ratio (IDR) at each floor is often used. This parameter is a global structure metric. To consolidate this into a unified directionless value, the resultant inter-storey drift is computed by employing the Square Root of the Sum of Squares (SRSS) combination technique, which combines the IDR values from the two orthogonal directions. Ultimately, the maximum inter-storey drift (MIRD) observed throughout the building is utilized as a singular *EDP* to quantify the demand sustained by the structures.

To capture localized damage, the Chord-Rotation Demand/Capacity Ratio (DCR) is determined for each local axis situated at the ends of the elements.

The Chord-Rotation Demand, which is schematically illustrated in Figure 7, is defined as the angle between the chord linking the analyzed end section of the member to the section on which the moment (M) equals zero, and the tangent to the member axis at the end section.

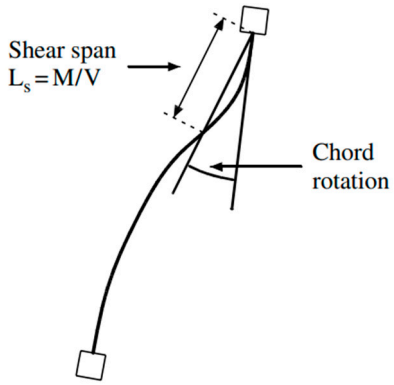

Figure 7. Chord-Rotation Demand.

Given that M is proportional to the curvature (φ), the section where $M = 0$ corresponds to the point of contraflexure within the member. Consequently, every structural element

is regarded as composed of two cantilevers anchored at the ends of the member. These cantilevers possess a length equivalent to the shear span (L_s), as defined in Equation (4):

$$L_s = M/V \tag{4}$$

If the nodal rotation at the targeted end of the member is relatively small compared to the drift of the corresponding equivalent cantilever, it becomes feasible to define the chord rotation as the deflection (D) at the end of the shear span divided by the shear span's length, as shown in Equation (5):

$$\theta_D = \frac{\Delta}{L_s} \tag{5}$$

The Chord-Rotation Capacity is calculated with the formulation explained in Equation (6):

$$\theta_u = \frac{1}{\gamma_{el}} 0.016 \cdot (0.3^{\nu}) \left[\frac{\max(0.01; \omega')}{\max(0.01; \omega)} f_c \right]^{0.225} \left(\frac{L_s}{h} \right)^{0.35} 25^{(\alpha \rho_{sx} \frac{f_{yw}}{f_c})} \left(1.25^{100 \rho_d} \right) \tag{6}$$

Further details about the other parameters for the formulations in use can be found in Eurocode 8 [9].

The choice to employ both Maximum Inter-Storey Drift Ratio (MIDR) and DCR is strategic. These metrics are in fact selected to provide a more comprehensive insight into both the local and global seismic behaviors of the reference structures.

3.3. Performance Level Selection

To construct fragility curves by utilizing DCR and MIDR as *EDPs*, as indicated in Section 3.2, two distinct Performance Levels (PL) are considered, following the ASCE 2012 guidelines: Life Safety (LS) and Collapse Prevention (CP) [30].

The *EDP* Life Safety thresholds are determined as three-quarters of the Collapse Prevention thresholds, adhering to the specified proportion. As for MIDR, the assumed capacity thresholds are established via pushover analysis. The threshold is ascertained by measuring the IDR of the first structural element where the demand-to-capacity ratio, concerning chord rotation, exceeds unity. This is aligned with the criteria from [8]. The MIDR_{PL} thresholds are summarized in Table 3.

Table 3. MIDR damage thresholds for CP and LS (%).

	RF	**NRF1**	**NRF2-Q2**	**NRF2-Q4**
MIDR CP	4.9	4.3	4.5	4.6
MIDR LS	3.7	3.3	3.4	3.5

Regarding DCR, the assumed capacity threshold is fixed at the value of 1, which corresponds to $\theta_D = \theta_u$. These approaches allow for the generation of fragility curves that provide insights into the structural response across different performance levels and seismic intensities. Table 4 summarizes the DCR_{PL} thresholds.

Table 4. DCR damage thresholds for CP and LS.

	RF	**NRF1**	**NRF2-Q2**	**NRF2-Q4**
DCR CP	1	1	1	1
DCR LS	0.75	0.75	0.75	0.75

3.4. Record Selection

Fragility assessment, as usual, is carried out based on the NLTHA results, and the Cloud Analysis procedure is preferred for developing fragility curves, due to its relatively lower computational demands [42]. Additionally, it relies on the utilization of unscaled ground motion records, thus mitigating potential biases introduced by scaling [43,44]. Usually, the number of records necessary for the estimation of fragility curves varies,

ranging from 40 to 100, depending on the chosen evaluation method [45–47]. In any case, several key aspects should be considered when selecting the records for Cloud Analysis [20]:

(i) the chosen records should span a wide range of the selected intensity measure, such as spectral acceleration values;
(ii) a substantial portion (approximately 30%) of the selected records should lead to an exceedance of the designated *EDP* limit state threshold (to minimize the need for extrapolation in regression);
(iii) the selection of more than 10% of the total records from the same seismic event should be avoided.

In this study, a collection of 61 unscaled strong ground motion records is taken into account from the European Strong Motion database [48].

A scatter plot illustrating the relationship between magnitude and distance for the selected records is presented in Figure 8. In the set of the 61 performed NLTHAs, the north–south component is consistently allocated to the *X* direction, while the east–west component is consistently assigned to the *Y* direction.

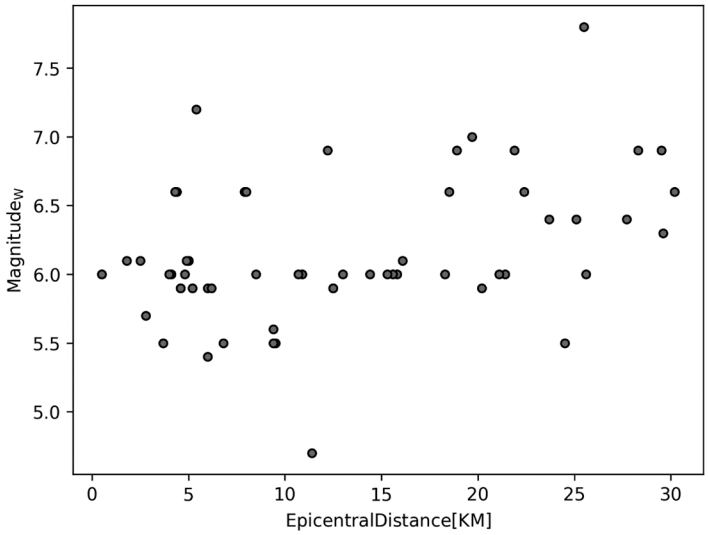

Figure 8. Magnitude–distance scatter plot for the selection of 61 ground motion records.

The elastic spectra of the selected records are provided in Figure 9.

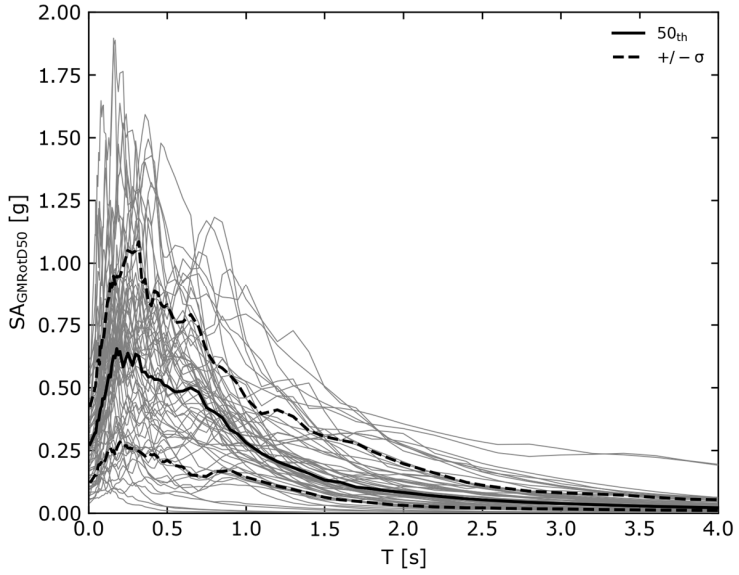

Figure 9. Elastic spectra of the selected records.

3.5. Fragility Development

It is important to note that the cautious selection of records for Cloud Analysis in relation to the Collapse Prevention Limit state may sometimes result in the selection of ground motions that could potentially induce structural collapse. Consequently, special consideration should be given to the structural response under such collapse-inducing records. This can be addressed explicitly through a Modified Cloud Analysis, as introduced by ref. [20]. For the purpose of this study, the focus remains on the original Cloud Analysis procedure, which does not encompass the consideration of so-called "collapse cases". Within this framework, the fragility function for a specific performance level can be expressed as follows [34,49]:

$$P\left(EDP > edp_{pl} \middle| IM\right) \tag{7}$$

Equation (7) means the probability of encountering an *EDP* that exceeds a given threshold value (edp_{pl}) given that an *IM* value occurred. This function can be computed using the standard cloud analysis approach, which operates under the assumption of a linear relationship between *EDP* and Intensity Measure (*IM*) within a bi-logarithmic plane:

$$\ln\left(edp|im\right) = a + b \cdot \ln(IM) \tag{8}$$

In Equation (8), $\ln(edp \mid im)$ represents the median estimate of the *EDP* given an *IM* value (*im*), while *a* and *b* denote the intercept on the *Y* axis and the slope of the regression line on the logarithmic scale, evaluated by applying the Ordinary Least Squares method. As per the hypothesis of the method, the residuals around the mean value are normally distributed with zero mean and constant logarithmic standard deviation, namely $\sigma_{\ln(EDP)|\ln(IM)}$, defined in Equation (9)

$$\sigma_{\ln(EDP)|\ln(IM)} = \sqrt{\left(\frac{\sum_n^1 (\ln(EDP_i) - \ln(edp_i|\, IM_i))^2}{N-2}\right)} \tag{9}$$

where *N* is the total number of records. Therefore, given an *EDP* threshold edp_{pl}, the probability of encountering *EDP* greater than edp_{pl} given *IM* follows a lognormal distribution, and it is defined in the following Equation (10):

$$P\left(EDP > edp_{pl} \middle| IM\right) = 1 - \Phi\left(\frac{\ln\left(edp_{pl}\right) - \ln(edp|IM)}{\sigma_{\ln(EDP)|\ln(IM)}}\right) \tag{10}$$

where Φ represents the cumulative distribution function of the standard normal distribution.

Fragility functions must be developed to incorporate the impact of uncertainties, as detailed in [31–33]. These uncertainties encompass various aspects, including the following: (i) variability from one record to another; (ii) variability in mechanical properties; (iii) variability in performance level capacity thresholds; (iv) uncertainties in model parameters; and (v) uncertainty in fragility median.

The first three sources can be primarily categorized as aleatory uncertainties, while the last one primarily pertains to epistemic uncertainty. The approach adopted in this study inherently addresses record-to-record variability, since each *IM-EDP* data pair, derived from the *N* NLTHAs, corresponds to a distinct record.

To address epistemic uncertainties, a bootstrap procedure is thus implemented [34,35,50]. This approach involves resampling with replacement of the initial data, resulting in *n* distinct linear regressions and fragility curves. In this study, a total of $n = 1000$ bootstraps is conducted.

Fragility median uncertainty can be understood as half of the logarithmic horizontal distance between the 16th and 84th percentiles of all *IM* values at 50% probability (median). This type of uncertainty is primarily epistemic and encapsulates the cumulative effect of uncertainties in all parameters of the fragility curves [50].

For this particular study, only record-to-record variability, uncertainties in model parameters and median fragility distributions are considered.

4. Discussion of the Results

For practical reasons, Figures 10 and 11 show only a selected example of typical $S_{a,avg}$—DCR correlation (linear regression) and the corresponding fragility curves, respectively. Figure 10 emphasizes the median regression values and the prediction interval (mean plus/minus one standard deviation), where each dot represents one among the *IM-EDP* couples. The median estimated parameters from the bootstrap procedure are also reported, with the gray lines showing the single bootstrap realizations. In these charts, a higher dispersion of the gray lines, i.e., the standard deviation $\sigma_{\ln(EDP)}$, signifies a more difficult prediction of the structural damage given the *IM*.

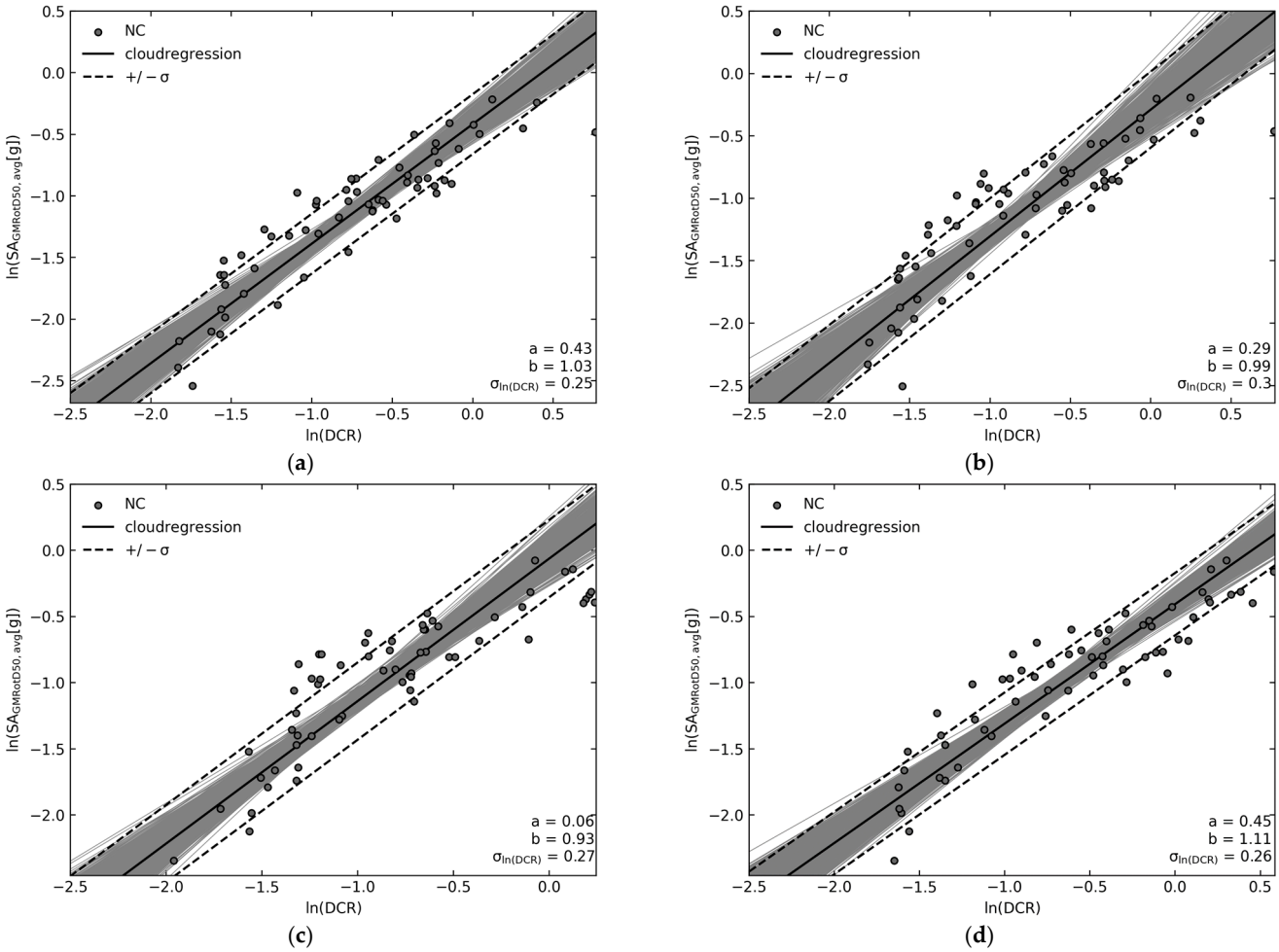

Figure 10. Linear regressions of the $S_{a,avg}$—DCR correlation for: (**a**) RF; (**b**) NRF1; (**c**) NRF2-Q2; and (**d**) NRF2-Q4.

Figure 11 shows the corresponding fragility curves. The red lines are the 50th percentile and the dotted lines are those for plus/minus one standard deviation. It can be noted that a higher standard deviation $\sigma_{\ln(EDP)}$ of linear regressions manifests in a higher dispersion of the fragility curves.

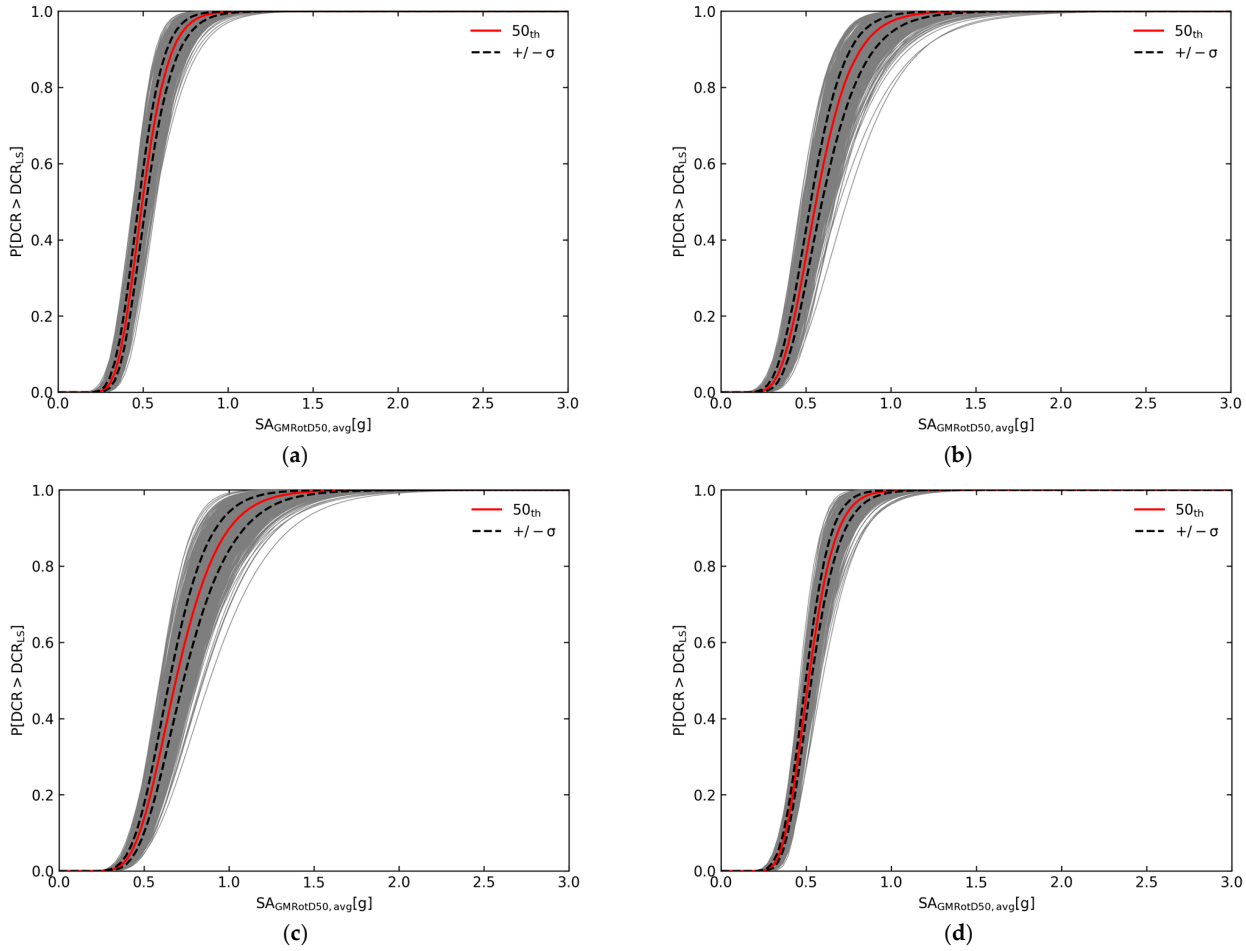

Figure 11. Fragility curves of the $S_{a,avg}$—DCR correlation for: (**a**) RF; (**b**) NRF1; (**c**) NRF2-Q2; and (**d**) NRF2-Q4.

Finally, the responses of all the examined RC structures are shown in Figure 12. The comparisons between the median linear regressions and the fragility curves are performed in order to assess the probability of exceeding the EDP_{PL} given a fixed *IM* value for the RC structures overall. In this way, it is easier to highlight the differences in the fragility functions among the reference structures.

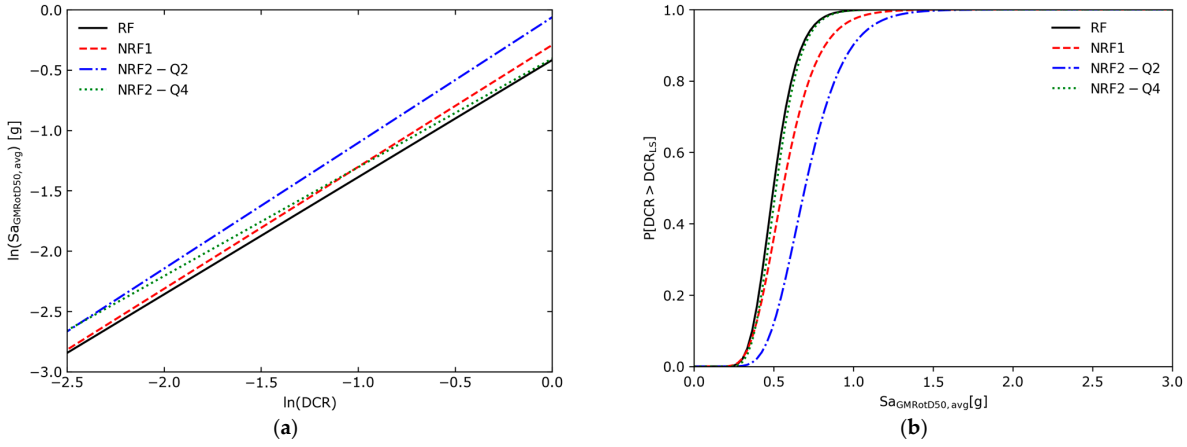

Figure 12. Comparisons of (**a**) median linear regressions and (**b**) fragility curves for the complete sample of accelerograms.

As shown in the figure, an increment in the irregularity of the structure does not correspond to a clear increment of the median fragility, which should indeed be expected to be consistent/proportional to the imposed non-regularity increment. The RF frame surprisingly appears to be the most vulnerable, while the NRF1 and NRF2-Q2 systems are remarkably less vulnerable. These results, in addition to being counterintuitive, are in contrast with what is shown by the structural analyses. In fact, looking at the raw *EDPs* obtained from the NLTH analysis, it is clear that the NRF2-Q4 frame has the highest number of EDPs exceeding the threshold EDP_{PL} compared to the other RC systems, as also summarized in Table 5. Hence, NRF2-Q4 should exhibit the highest fragility.

Table 5. Amount of $EDP > EDP_{PL}$ for individual RC frames.

	RF	NRF1	NRF2-Q2	NRF2-Q4
$EDP > EDP_{CP}$	6	6	7	12
$EDP > EDP_{LS}$	16	13	12	21

In the fragility assessment from Cloud Analysis procedure, if the *IM-EDP* couples are largely located away from the EDP_{PL}, it is easy to incur biased extrapolation of the linear regression and, therefore, of the fragility curve determination. To try to explain the above-mentioned inconsistency, the total amount of accelerograms is reduced to thirty-one accelerograms, which show *EDPs* evenly distributed around the *EDP* threshold for the Life Safety performance level. Hence, the methodology was re-applied to this reduced dataset. This strategy was followed to account for possible bias in the record selection process. In the latter case, the linear regressions and the fragility curves were made without bootstrapping. Figure 13 shows the corresponding results. As can be seen in the figure, the results still agree with the previous analysis.

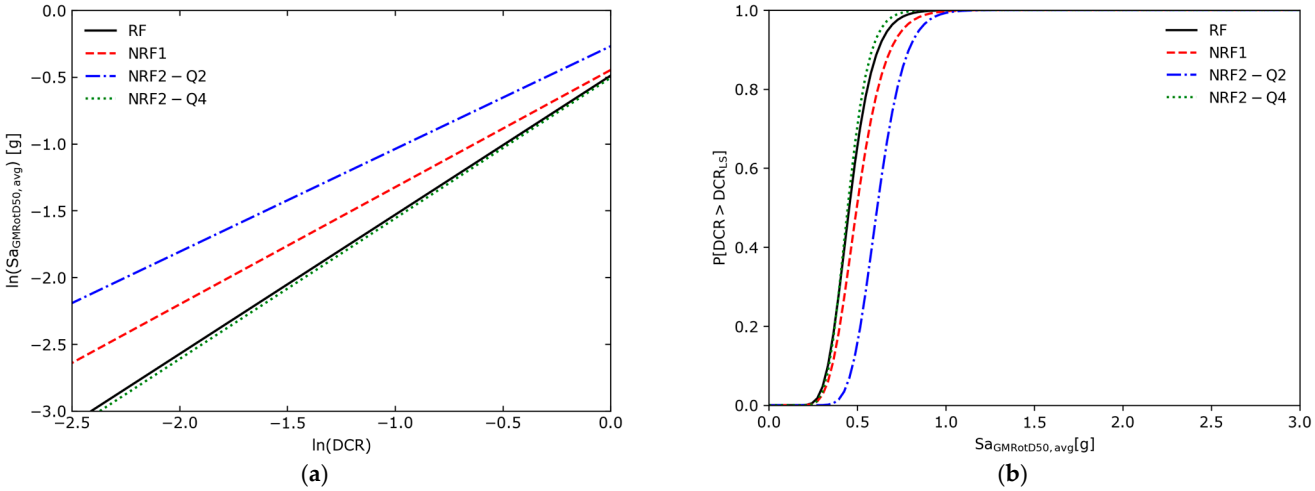

(**a**) (**b**)

Figure 13. Comparison of (**a**) linear regressions and (**b**) fragility curves for the reduced sample of accelerograms.

Since both previous analyses seem in contrast with the raw data, the last investigation regards the applied statistical model for the fragility development. Hence, in order to understand whether the results of the fragility analysis are due to the inability of the statistical model to represent them, a logistic regression based on a maximum likelihood estimation is finally applied to both whole and reduced samples of accelerograms [20]. It is worth noting that the logistic regression model falls under the category of generalized regression models, and it proves especially valuable in situations in which the dependent variable is binary. In this context, binary means that the variable can only take on two values, typically represented as 1 and 0, akin to "yes" or "no". This binary nature aligns

perfectly with the *C* (collapse) and *NC* (no collapse) categories of the structural response, as seen in ref. [20]. Equation (11) shows the probability of collapse:

$$P(C|IM) = \frac{1}{1 + e^{-(\alpha_0 + \alpha_1 \cdot \ln(IM))}} \quad (11)$$

where α_0 and α_1 are the parameters of the logistic regression. In this study, the logistic regression model is applied across all the correlations, but instead of evaluating the probability of collapse, the correlations are differentiated by the outcomes of 1 or 0, depending on whether they result in *EDPs* exceeding the EDP_{LS} (Life Safety) threshold. The curves obtained in this way for the complete set of accelerograms are shown in Figure 14. Here, both regression and data dots, i.e., couples (*IM*, 0) and (*IM*, 1), are illustrated. The comparison among these regression curves (fragility curves) is shown in Figure 15, where the regression curve of the RF structure still shows the highest fragility, and the NRF2-Q2 the lowest.

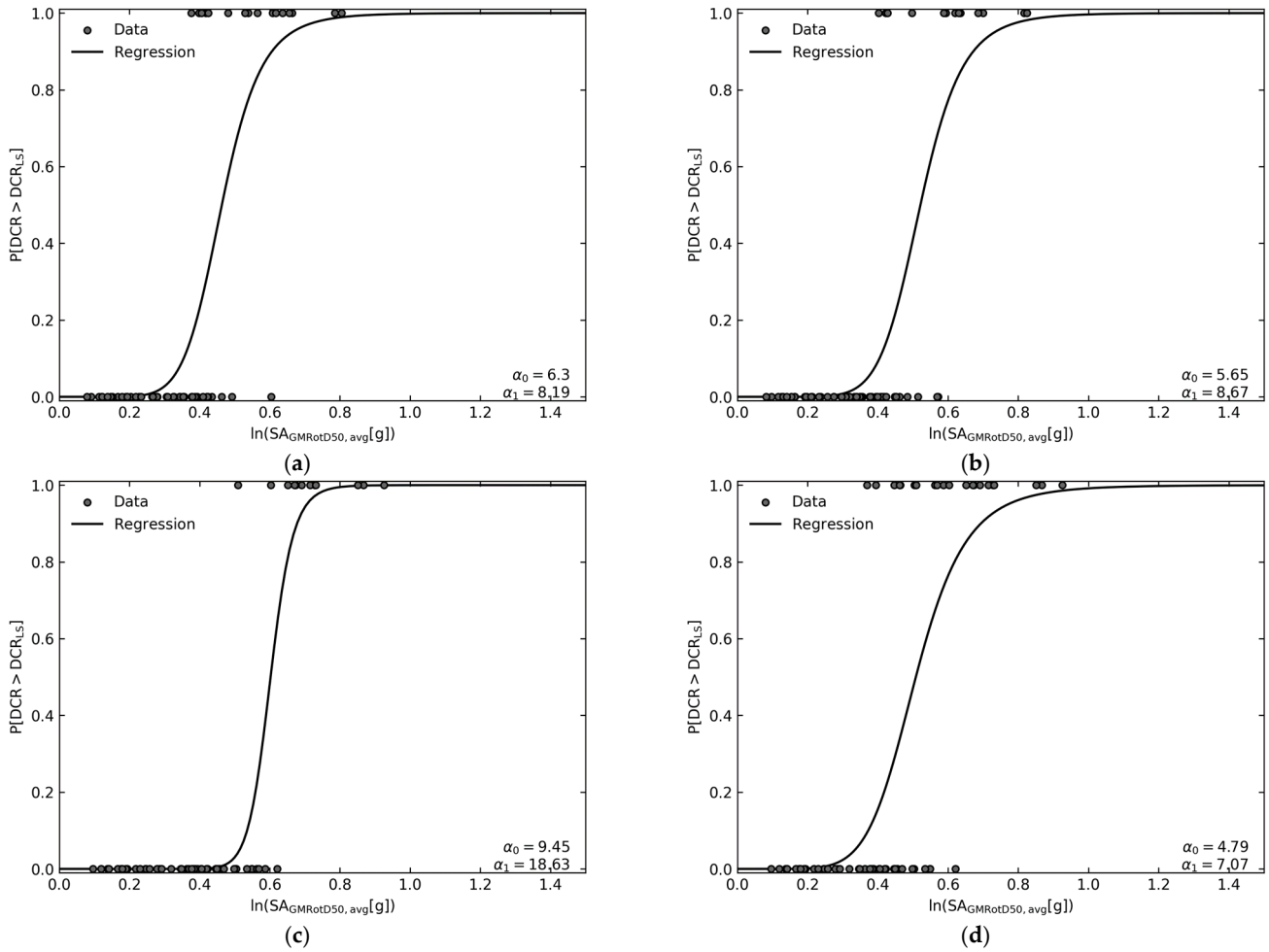

Figure 14. Logistic regression for the complete sample of accelerograms for (**a**) RF; (**b**) NRF1; (**c**) NRF2-Q2; and (**d**) NRF2-Q4.

As a last step, the logistic regression was then applied to the reduced sample of input accelerograms, and the typical results can be seen in Figure 16. Figure 17 presents the comparison of the logistic regressions obtained with the reduced subset of accelerograms. Figure 16 highlights, in more detail, that a significant part of the $EDP < EDP_{LS}$ dots (i.e., outcome of 0) corresponds to an *IM* value equal to the dots that have the outcome of 1. Moreover, in Figure 17, the fragility related to the RF structure is still the highest. Clearly, the logistic model applied to both the whole and the reduced sample does not show the

consistency/proportion between fragility and structural non-regularity for the examined RC frames. Similar results are obtained using other intensity measures.

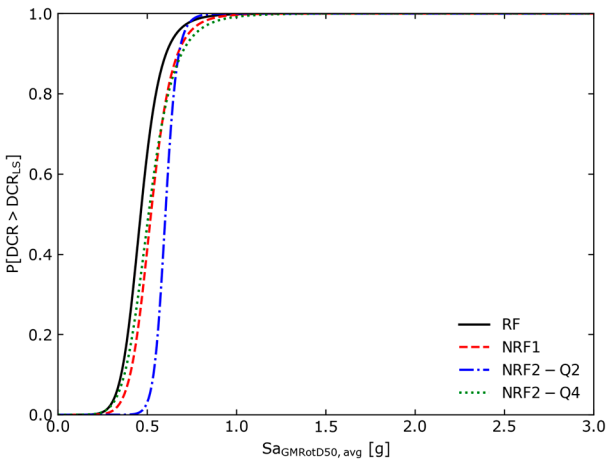

Figure 15. Comparison of logistic regressions for the complete sample of accelerograms.

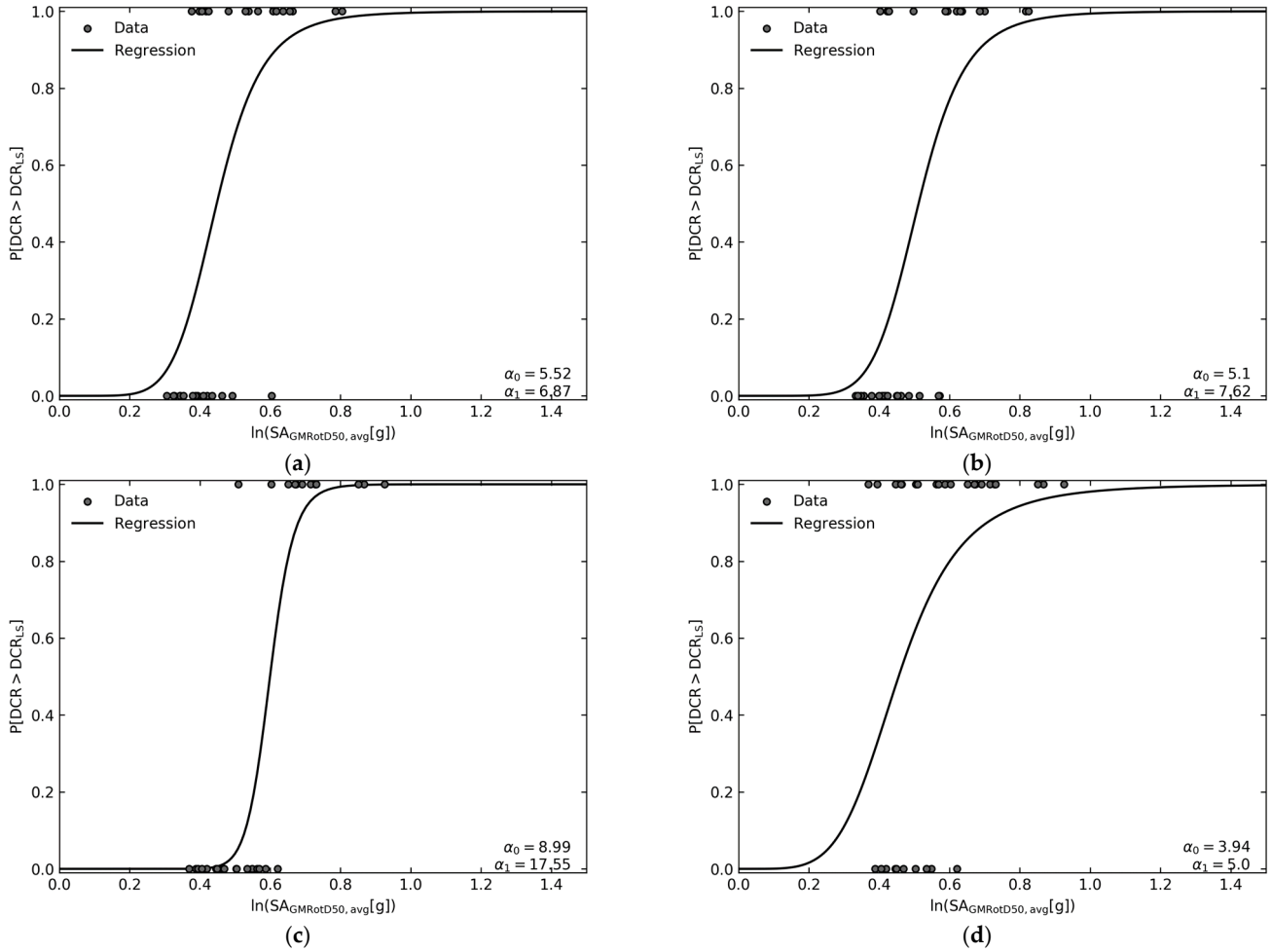

Figure 16. Logistic regressions for the reduced sample of accelerograms for (**a**) RF; (**b**) NRF1; (**c**) NRF2-Q2; and (**d**) NRF2-Q4.

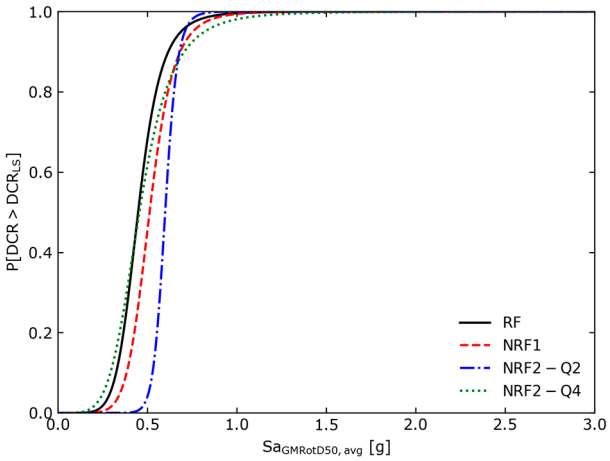

Figure 17. Comparison of the logistic regressions for the reduced sample of accelerograms.

5. Conclusions

In this study, the seismic performances of non-regular reinforced concrete (RC) frames were numerically investigated. In particular, linear and logistic regression analyses and fragility curves—generated using the Cloud Analysis procedure—were presented. These analyses were carried out on a selection of a total of four three-dimensional (3D) RC frames characterized by varying levels of in-plan and in-height non-regularities. Furthermore, it is important to note that the examined structures were conceived to maintain comparable levels of design safety. The locations of these structures was assumed in a high-seismicity region, and their design was performed to adhere to the Italian NTC2018 code.

The numerical study employed a set of 61 unscaled recorded ground motions, which were selected by following the procedure outlined in ref. [20]. Three different Intensity Measures (*IMs*) and two Engineering Demand Parameters (*EDPs*) were considered for establishing the correlation in linear regression. Furthermore, to address epistemic uncertainties, a bootstrap procedure was implemented.

Interestingly, it was shown that the numerical results of the fragility curves do not align with the anticipated increase in damage, due to the imposed structural non-regularity. This discrepancy was particularly pronounced when the raw *EDPs* were examined. In an attempt to mitigate potential biases stemming from the initial record selection, linear regressions and fragility curves were also devised for a reduced subset of accelerograms. However, the comparative outcomes exhibited minimal differences and were found to be mostly in line with previous outcomes. Consequently, logistic regression was also applied to both the complete dataset and the reduced subset of accelerograms. The goal was to capture any underlying behavior, but also, in this case, the collected numerical results did not align with the expected increase in damage due to the non-regularity of the examined buildings.

To some extent, the presented findings suggest that code-conforming structures, regardless of their regularity, show similar fragilities. This may be a consequence of the response spectrum analysis used in the design of the structures, in which a higher spectral acceleration is used for the design of beams and columns for all structures with a lower vibration period. This may also partially compensate for the torsional effects. In this regard, it is important to highlight that the Italian Building Code takes additional precautions by reducing the overall amount of seismic energy being dissipated (by using a q-factor equal to 2) for buildings characterized by high in-plant irregularities.

The results of the present analyses support this statement, given that the NRF2-Q2 structure always shows the less fragility. However, some differences in fragility among the RF and NRF2-Q4 were expected, and this incongruity with raw damage response data might find its justification in seismological considerations and in the intricacies of statistical

modeling. A single scalar intensity measure, even if properly selected, can be an efficient, but not an exhaustive, representation of the ground motion.

Hence, the presented comparative results suggest that linear and logistic regression models may not be the most suitable statistical tools for correlating *EDPs* with *IMs*, which may not be sufficient to represent the input ground motion. Therefore, all these aspects warrant in-depth exploration in future extended studies. Moreover, it is important to note that the lack of availability of enough strong records also affects the record selection [51,52]. For this reason, the use of synthetic physics-based ground motion simulations can boost the methodology, as detailed in refs. [53,54]. Further investigations will be carried out in this direction.

Author Contributions: M.F.: Conceptualization, methodology, software, validation, writing—original draft preparation; G.S.: formal analysis, investigation, data curation, writing—original draft preparation. C.B.: resources, writing—original draft preparation, funding acquisition. All authors have read and agreed to the published version of the manuscript.

Funding: This research activity was partially funded by DPC-ReLUIS project ("Mappe di rischio e scenari di danno sismico (MARS)—WP4, UR: TS"). DPC-ReLUIS is gratefully acknowledged for providing financial support to the University of Trieste team members.

Data Availability Statement: The datasets presented in this article are not readily available because the data are part of an ongoing study. Requests to access the datasets should be directed to the authors.

Conflicts of Interest: The authors declare no conflicts of interest.

References

1. Chopra, A.K. *Dynamics of Structures–Theory and Applications to Earthquake Engineering, Fifth Edition in SI Units*; Pearson: London, UK, 2020.
2. Fardis, M.N. *Seismic Design, Assessment and Retrofitting of Concrete Buildings*; Springer: Dordrecht, The Netherlands, 2009.
3. Anderson, R.W. The San Salvador Earthquake of October 10, 1986—Review of building damage. *Earthq. Spectra* **1987**, *3*, 497–541. [CrossRef]
4. Ellingwood, B.; Brady, A.G. *An Investigation of the Miyagi-Ken-Oki, Japan, Earthquake of June 12, 1978*; National Institute of Standards and Technology: Gaithersburg, MD, USA, 1980.
5. Elnashai, A.S.; Gencturk, B.; Kwon, O.-S.; Al-Qadi, I.L.; Hashash, Y.; Roesler, J.R.; Kim, S.J.; Jeong, S.-H.; Dukes, J.; Valdivia, A. *The Maule (Chile) Earthquake of February 27, 2010: Consequence Assessment and Case Studies*; Mid-America Earthquake Center: Urbana-Champaign, IL, USA, 2010.
6. Rosenblueth, E. *The 1985 Earthquake: Causes and Effects in Mexico City*; National Reconstruction Commission, Committee Mexico City's Metropolitan Area: Mexico City, Mexico, 1986.
7. ICC. 2018 IBC SEAOC Structural/Seismic Design Manual Volume 3: Examples for Concrete Buildings: ICC: 9781609839987. Dubai: United Arab Emirates. Available online: https://www.amazon.com/SEAOC-Structural-Seismic-Design-Manual/dp/1609839986 (accessed on 20 November 2024).
8. Ministero delle Infrastrutture e dei Trasporti, Governo della Repubblica Italiana. Aggiornamento delle: Norme tecniche per le costruzioni. *Gazz. Uff. Repubb. Ital.* **2018**. Available online: https://www.gazzettaufficiale.it/eli/id/2018/2/20/18A00716/sg (accessed on 20 November 2024).
9. *CEN. EN 1998-3*; Eurocode 8: Design of Structures for Earthquake Resistance–Part 3: Assessment and Retrofitting of Buildings. European Committee for Standardization (CEN): Brussels, Belgium, 2005.
10. Rota, M.; Penna, A.; Strobbia, C.L. Processing Italian damage data to derive typological fragility curves. *Soil Dyn. Earthq. Eng.* **2008**, *28*, 933–947. [CrossRef]
11. Lagomarsino, S.; Giovinazzi, S. Macroseismic and mechanical models for the vulnerability and damage assessment of current buildings. *Bull. Earthq. Eng.* **2006**, *4*, 415–443. [CrossRef]
12. Del Gaudio, C.; De Martino, G.; Di Ludovico, M.; Manfredi, G.; Prota, A.; Ricci, P.; Verderame, G.M. Empirical fragility curves for masonry buildings after the 2009 L'Aquila, Italy, Earthquake. *Bull. Earthq. Eng.* **2019**, *17*, 6301–6330. [CrossRef]
13. Moon, D.-S.; Lee, Y.-J.; Lee, S. Fragility analysis of space reinforced concrete frame structures with structural irregularity in plan. *J. Struct. Eng.* **2018**, *144*, 04018096. [CrossRef]
14. Yuen, Y.P.; Kuang, J.S. Nonlinear seismic responses and lateral force transfer mechanisms of RC frames with different infill configurations. *Eng. Struct.* **2015**, *91*, 125–140. [CrossRef]
15. Valente, M. Seismic upgrading strategies for non-ductile plan-wise irregular R/C structures. *Procedia Eng.* **2013**, *54*, 539–553. [CrossRef]

16. Khanal, B.; Chaulagain, H. Seismic elastic performance of L-shaped building frames through plan irregularities. *Structures* **2020**, *27*, 22–36. [CrossRef]
17. Özmen, G.; Girgin, K.; Durgun, Y. Torsional irregularity in multi-story structures. *Int. J. Adv. Struct. Eng.* **2014**, *6*, 121–131. [CrossRef]
18. Amarloo, N.; Emami, A.R. A 3-dimensional perspective for inter-storey drift, ductility and damage distributions in plan-irregular RC buildings considering seismic orientation effect. *Bull. Earthq. Eng.* **2019**, *17*, 3447–3474. [CrossRef]
19. Luco, N.; Cornell, C.A. Structure-specific scalar intensity measures for near-source and ordinary earthquake ground motions. *Earthq. Spectra* **2007**, *23*, 357–392. [CrossRef]
20. Jalayer, F.; Ebrahimian, H.; Miano, A.; Manfredi, G.; Sezen, H. Analytical fragility assessment using unscaled ground motion records. *Earthq. Eng. Struct. Dyn.* **2017**, *46*, 2639–2663. [CrossRef]
21. Ebrahimian, H.; Jalayer, F. Selection of seismic intensity measures for prescribed limit states using alternative nonlinear dynamic analysis methods. *Earthq. Eng. Struct. Dyn.* **2021**, *50*, 1235–1250. [CrossRef]
22. Federal Emergency Management Agency. *FEMA Assessing Seismic Performance of Buildings with Configuration Irregularities*; FEMA P-2012; Applied Technology Council for the Federal Emergency Management Agency: Washington, DC, USA, 2018.
23. Smiroldo, G.; Fasan, M.; Bedon, C. Non-regularity damage evaluation in reinforced concrete structures via fragility curves. *Vibroeng. Procedia* **2023**, *50*, 28–34. [CrossRef]
24. Smiroldo, G.; Fasan, M.; Amadio, C. Fragility curves for reinforced concrete frames characterised by different regularity. *Procedia Struct. Integr.* **2023**, *44*, 283–290. [CrossRef]
25. American Society of Civil Engineers. *Minimum Design Loads and Associated Criteria for Buildings and Other Structures*; American Society of Civil Engineers: Reston, VA, USA, 2020.
26. Seismosoft. *SeismoStruct 2023*, Seismosoft: Pavia, Italy, 2023.
27. Mander, J.B.; Priestley, M.J.N.; Park, R. Theoretical stress-strain model for confined concrete. *J. Struct. Eng.* **1988**, *114*, 1804–1826. [CrossRef]
28. Menegotto, M.; Pinto, P.E. Method of analysis for cyclically loaded R.C. plane frames including changes in geometry and non-elastic behaviour of elements under combined normal force and bending. In *Symposium on the Resistance and Ultimate Deformability of Structures Acted on by Well Defined Repeated Loads*; IABSE: Zurich, Switzerland, 1973; pp. 15–22.
29. Barbagallo, F.; Bosco, M.; Marino, E.M.; Rossi, P.P. On the fibre modelling of beams in RC framed buildings with rigid diaphragm. *Bull. Earthq. Eng.* **2020**, *18*, 189–210. [CrossRef]
30. *ASCE/SEI 41-13*; Seismic Evaluation and Retrofit of Existing Buildings. American Society of Civil Engineers (ASCE): Reston, VA, USA, 2012.
31. Pitilakis, K.; Crowley, E.; Crowley, E. *SYNER-G: Typology Definition and Fragility Functions for Physical Elements at Seismic Risk*; Springer: Dordrecht, The Netherlands, 2014.
32. Bakalis, K.; Vamvatsikos, D. Seismic fragility functions via nonlinear response history analysis. *J. Struct. Eng.* **2018**, *144*, 04018181. [CrossRef]
33. Silva, V.; Akkar, S.; Baker, J.; Bazzurro, P.; Castro, J.M.; Crowley, H.; Dolsek, M.; Galasso, C.; Lagomarsino, S.; Monteiro, R.; et al. Current challenges and future trends in analytical fragility and vulnerability modeling. *Earthq. Spectra* **2019**, *35*, 1927–1952. [CrossRef]
34. Fasan, M. *Develop Fragility Curves as a Function of Intensity for Full SRA in Intensity Domain. Work Package 6 Ground-Motion for Engineers*; SIGMA-2 Project: Marseille, France, 2021.
35. Iervolino, I. Assessing uncertainty in estimation of seismic response for PBEE. *Earthq. Eng. Struct. Dyn* **2017**, *46*, 1711–1723. [CrossRef]
36. Boore, D.M. Orientation-independent measures of ground motion. *Bull. Seismol. Soc. Am.* **2006**, *96*, 1502–1511. [CrossRef]
37. Eads, L.; Miranda, E.; Lignos, D.G. Average spectral acceleration as an intensity measure for collapse risk assessment. *Earthq. Eng. Struct. Dyn.* **2015**, *44*, 2057–2073. [CrossRef]
38. Kohrangi, M.; Bazzurro, P.; Vamvatsikos, D. Vector and scalar IMs in structural response estimation, Part I: Hazard analysis. *Earthq. Spectra* **2016**, *32*, 1507–1524. [CrossRef]
39. Ebrahimian, H.; Jalayer, F.; Lucchini, A.; Mollaioli, F.; Manfredi, G. Preliminary ranking of alternative scalar and vector intensity measures of ground shaking. *Bull. Earthq. Eng.* **2015**, *13*, 2805–2840. [CrossRef]
40. Kazantzi, A.K.; Vamvatsikos, D. Intensity measure selection for vulnerability studies of building classes. *Earthq. Eng. Struct. Dyn.* **2015**, *44*, 2677–2694. [CrossRef]
41. Kohrangi, M.; Vamvatsikos, D.; Bazzurro, P. Implications of intensity measure selection for seismic loss assessment of 3-D buildings. *Earthq. Spectra* **2016**, *32*, 2167–2189. [CrossRef]
42. Mattei, S.; Fasan, M.; Bedon, C. On the use of cloud analysis for structural glass members under seismic events. *Sustainability* **2021**, *13*, 9291. [CrossRef]
43. Luco, N.; Bazzurro, P. Does amplitude scaling of ground motion records result in biased nonlinear structural drift responses? *Earthq. Eng. Struct. Dyn.* **2007**, *36*, 1813–1835. [CrossRef]
44. Zacharenaki, A.; Fragiadakis, M.; Assimaki, D.; Papadrakakis, M. Bias assessment in incremental dynamic analysis due to record scaling. *Soil Dyn. Earthq. Eng.* **2014**, *67*, 158–168. [CrossRef]

45. Hancock, J.; Bommer, J.J.; Stafford, P.J. Numbers of scaled and matched accelerograms required for inelastic dynamic analyses. *Earthq. Eng. Struct. Dyn.* **2008**, *37*, 1585–1607. [CrossRef]
46. Baltzopoulos, G.; Baraschino, R.; Iervolino, I. On the number of records for structural risk estimation in PBEE. *Earthq. Eng. Struct. Dyn.* **2018**, *48*, 489–506. [CrossRef]
47. Kiani, J.; Camp, C.; Pezeshk, S. On the number of required response history analyses. *Bull. Earthq. Eng.* **2018**, *16*, 5195–5226. [CrossRef]
48. Luzi, L.; Lanzano, G.; Felicetta, C.; D'Amico, M.C.; Russo, E.; Sgobba, S.; Pacor, F. *ORFEUS Working Group 5 Engineering Strong Motion Database (ESM) (Version 2.0)*; Istituto Nazionale di Geofisica e Vulcanologia (INGV): Rome, Italy, 2020.
49. Jalayer, F.; Cornell, C.A. Alternative non-linear demand estimation methods for probability-based seismic assessments. *Earthq. Eng. Struct. Dyn.* **2009**, *38*, 951–972. [CrossRef]
50. Jalayer, F.; Ebrahimian, H.; Miano, A. Record-to-record variability and code-compatible seismic safety-checking with limited number of records. *Bull. Earthq. Eng.* **2021**, *19*, 6361–6396. [CrossRef]
51. Paolucci, R.; Gatti, F.; Infantino, M.; Smerzini, C.; Güney Özcebe, A.; Stupazzini, M. Broadband ground motions from 3D physics-based numerical simulations using artificial neural networks. *Bull. Seismol. Soc. Am.* **2018**, *108*, 1272–1286. [CrossRef]
52. Smerzini, C.; Amendola, C.; Paolucci, R.; Bazrafshan, A. Engineering validation of BB-SPEEDset, a data set of near-source physics-based simulated accelerograms. *Earthq. Spectra* **2024**, *40*, 420–445. [CrossRef]
53. Chieffo, N.; Fasan, M.; Romanelli, F.; Formisano, A.; Mochi, G. Physics-based ground motion simulations for the prediction of the seismic vulnerability of masonry building compounds in Mirandola (Italy). *Buildings* **2021**, *11*, 667. [CrossRef]
54. Hassan, H.M.; Fasan, M.; Sayed, M.A.; Romanelli, F.; ElGabry, M.N.; Vaccari, F.; Hamed, A. Site-specific ground motion modeling for a historical Cairo site as a step towards computation of seismic input at cultural heritage sites. *Eng. Geol.* **2020**, *268*, 105524. [CrossRef]